





**Benchmarking boron carbide equation of state using computation and experiment**

Shuai Zhang <sup>1,2,\*</sup> Michelle C. Marshall <sup>1,†</sup> Lin H. Yang,<sup>1</sup> Philip A. Sterne,<sup>1</sup> Burkhard Militzer,<sup>3,4,‡</sup> Markus Däne <sup>1</sup>,  
James A. Gaffney,<sup>1</sup> Andrew Shamp,<sup>1</sup> Tadashi Ogitsu,<sup>1</sup> Kyle Caspersen,<sup>1</sup> Amy E. Lazicki,<sup>1</sup> David Erskine <sup>1</sup>,  
Richard A. London,<sup>1</sup> Peter M. Celliers,<sup>1</sup> Joseph Nilsen,<sup>1</sup> and Heather D. Whitley<sup>1,§</sup>

<sup>1</sup>Lawrence Livermore National Laboratory, Livermore, California 94550, USA

<sup>2</sup>Laboratory for Laser Energetics, University of Rochester, Rochester, New York 14623, USA

<sup>3</sup>Department of Earth and Planetary Science, University of California, Berkeley, California 94720, USA

<sup>4</sup>Department of Astronomy, University of California, Berkeley, California 94720, USA



(Received 1 August 2020; accepted 8 October 2020; published 3 November 2020)

Boron carbide ( $B_4C$ ) is of both fundamental scientific and practical interest due to its structural complexity and how it changes upon compression, as well as its many industrial uses and potential for use in inertial confinement fusion (ICF) and high-energy density physics experiments. We report the results of a comprehensive computational study of the equation of state (EOS) of  $B_4C$  in the liquid, warm dense matter, and plasma phases. Our calculations are cross-validated by comparisons with Hugoniot measurements up to 61 megabar from planar shock experiments performed at the National Ignition Facility (NIF). Our computational methods include path integral Monte Carlo, activity expansion, as well as all-electron Green's function Korringa-Kohn-Rostoker and molecular dynamics that are both based on density functional theory. We calculate the pressure-internal energy EOS of  $B_4C$  over a broad range of temperatures ( $\sim 6 \times 10^3$ – $5 \times 10^8$  K) and densities ( $0.025$ – $50$  g/cm<sup>3</sup>). We assess that the largest discrepancies between theoretical predictions are  $\lesssim 5\%$  near the compression maximum at  $1$ – $2 \times 10^6$  K. This is the warm-dense state in which the K shell significantly ionizes and has posed grand challenges to theory and experiment. By comparing with different EOS models, we find a Purgatorio model (LEOS 2122) that agrees with our calculations. The maximum discrepancies in pressure between our first-principles predictions and LEOS 2122 are  $\sim 18\%$  and occur at temperatures between  $6 \times 10^3$ – $2 \times 10^5$  K, which we believe originate from differences in the ion thermal term and the cold curve that are modeled in LEOS 2122 in comparison with our first-principles calculations. To account for potential differences in the ion thermal term, we have developed three new equation-of-state models that are consistent with theoretical calculations and experiment. We apply these new models to 1D hydrodynamic simulations of a polar direct-drive NIF implosion, demonstrating that these new models are now available for future ICF design studies.

DOI: [10.1103/PhysRevE.102.053203](https://doi.org/10.1103/PhysRevE.102.053203)

**I. INTRODUCTION**

The design of high-energy density and inertial confinement fusion (ICF) experiments requires a good description of the ablator equation of state (EOS). Materials that are typically used as ablators are plastics, such as hydrocarbons (CH) and glow discharge polymers (GDP) [1–4]. However, formation of condensed phase microstructures and mixing with the DT fuel during implosion could affect the performance of the ignition target [5,6]. Additional materials with higher density and hardness, such as high-density carbon (HDC), boron-materials, and beryllium also provide current and future options for ablators [7–12]. In comparison to plastics, these high-tensile strength materials typically exhibit ablation pressures that are 15–20% higher [8]. Using these materials as the ablator can have higher x-ray absorption and use a shorter

laser pulse with a higher ablation rate for a given temperature, and thereby require a thinner ablator shell while maintaining the same mass and outer diameter [8,11,13]. Ablators doped with boron have also been the subject of more recent proposals to use reactions with  $\gamma$  rays as a means of quantifying ablator mix in ICF experiments [14], and boron carbide is of particular interest for ignition experiments because a method for producing hollow capsules has already been demonstrated [15].

In recent studies, Zhang *et al.* combined several computational methods to set accurate constraint for the EOS of boron (B) [13] and boron nitride (BN) [16] over a wide range of temperatures ( $\sim 0.2$  eV–50 keV) and densities (0.1–20 times compression). They also conducted laser shock experiments at the Omega laser facility and the National Ignition Facility (NIF) to measure the Hugoniot EOS to pressures of 10–60 megabar (Mbar) and demonstrated remarkable agreement with the first-principles predictions. Their data have enabled building new EOS tables (X52 for B and X2152 for BN) based on the quotidian EOS (QEOS) model [17,18] and clarifying the dominating physics (cold curve, ion thermal, or electron thermal) at different regions of the temperature-density space.

\*szha@lle.rochester.edu

†marshall47@llnl.gov

‡militzer@berkeley.edu

§whitley3@llnl.gov

They also performed 1D hydrodynamic simulations of polar direct-drive exploding-pusher experiments [19] to explore the performance sensitivity to the EOS.

Boron carbide is another important member in the family of boron materials. At ambient condition, it has a high melting point, superior hardness, low specific weight, good resistance to chemical agents, and high neutron absorption cross section. These outstanding properties allow it to be widely used for mechanical, electrical, chemical, and nuclear applications [20]. The ambient crystal structure of  $B_4C$  has rhombohedral symmetry (space group  $R\bar{3}m$ ), similar to that of  $\alpha$ -B, and is characterized by B-rich icosahedra and C-rich chains. X-ray diffraction experiments reveal this structure to be stable under static compression at up to 126 GPa [21]. Single-crystal experiments show that the icosahedral units are less compressible than the unit cell volume and the static compression is governed by force transfer between the rigid icosahedra [22]. However, dramatic structural changes have been reported under shock compression [23–25], scratching and nanoindentation [26–28], or depressurization [29] and attributed to amorphization or structural transition that is accompanied by changes in hardness, compressibility, or elastic modulus [23,30,31]. There have also been studies that show the shear strength of boron-rich boron carbide can be lowered due to nanotwins [32] and multiscale molecular dynamics (MD) simulations that relate structural changes to hydrostaticity of compression [33].

Over the past few years, knowledge about the EOS of boron carbide has advanced significantly. The EOS and melting curve of  $B_4C$  were constructed by Molodets *et al.* [34] that agree with available experiments at up to megabar pressures, featuring melting with a negative Clapeyron slope at pressures below 150 GPa and a positive one above 170 GPa. Jay *et al.* [35] performed comprehensive *ab initio* calculations for boron carbide at up to 80 GPa and 2000 K, and their temperature-pressure-concentration phase diagrams show phase separation of boron carbides in multiple stages and into B and C at above 70 GPa. Fratanduono *et al.* [36] extended the Hugoniot, sound velocities, and thermodynamic properties measurements of liquid  $B_4C$  to 700 GPa. Shamp *et al.* [37] performed MD calculations based on density functional theory (DFT) to determine the Hugoniot curve up to 1500 GPa, and predicted discontinuities along the Hugoniot at <100 GPa as results of phase separation and transformation in solid  $B_4C$ . An equation-of-state table (LEOS 2122) based on an average atom-in-jellium model (Purgatorio) [38] has thus been developed that fits all available experimental Hugoniot data above 100 GPa [36]. However, accurate EOS at higher pressures and temperatures, in particular those corresponding to the partially ionized, warm dense state, is still unknown.

The goal of this work is to benchmark the EOS of  $B_4C$  in a wide range of temperatures and pressures by combining theoretical calculations and experiments. Our theoretical methods include path integral Monte Carlo (PIMC), pseudopotential DFT-MD approaches realized in multiple schemes, an activity expansion method (ACTEX), and an all-electron, Green's function Korringa-Kohn-Rostoker (KKR) method. Our experiments consist of seven Hugoniot measurements conducted at the NIF. The paper is organized as follows: Sec. II outlines our computational details; Sec. III describes our shock

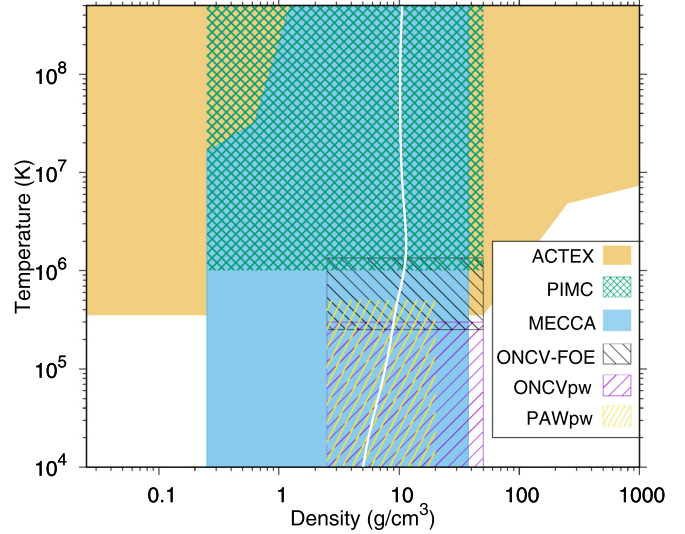


FIG. 1. Schematic diagram showing the temperature-density regions at which different methods are used in this work for calculating the EOS of  $B_4C$ . The principal Hugoniot from LEOS 2122 is shown (white curve) for comparison.

experiments; Sec. IV compares our EOS and Hugoniot results from computation and experiments, constructs new EOS models, and explores the role of EOS in hydrodynamic simulations; Sec. V discusses the microscopic physics of  $B_4C$  by combining electronic structure and QEOS perspectives; finally we conclude in Sec. VI.

## II. COMPUTATIONAL METHODS

In this section, we briefly describe the computational settings of the theoretical methods that we employ to compute the internal energies and pressures of  $B_4C$  across wide ranges of temperatures and densities. Figure 1 summarizes the conditions at which each of the methods has been used. The computations are performed by leveraging the applicability, accuracy, and efficiency of each method. More theoretical details can be found in our recent paper [16] and references therein.

We perform PIMC simulations of  $B_4C$  using the CUPID code [39]. All electrons and nuclei are treated explicitly. To deal with the Fermionic sign problem, we apply the fixed-node approximation using free-particle nodes to restrict the paths [40–42]. The pair density matrices [43,44] are evaluated in steps of  $\frac{1}{512}$  Hartree $^{-1}$  ( $\text{Ha}^{-1}$ ) and the nodal restriction is enforced in steps of  $\frac{1}{8192}$   $\text{Ha}^{-1}$ . The calculations are performed at densities of 0.25–50.17  $\text{g}/\text{cm}^3$  [0.1 to 20 times the ambient density ( $\rho_0 \sim 2.5 \text{ g}/\text{cm}^3$ ) [45]] and temperatures of  $10^6$ – $5 \times 10^8$  K. Each simulation cell consists of 30 atoms, which is comparable to our previous simulations for pure B, BN, and hydrocarbons [13,16,46,47]. By comparing the EOS and the radial distribution function  $g(r)$  obtained using 30-atom cells to those using 120-atom cells in our DFT-MD calculations, we find negligible differences at temperatures above  $5 \times 10^4$  K [a comparison in  $g(r)$  is shown in Fig. 9]. We therefore assert that the finite cell size effects on the EOS are negligible at such high temperature conditions.

Our DFT-MD simulations for  $B_4C$  are performed in two different ways. One way is by using the frozen-1s-core projector augmented wave (PAW) [48] or optimized norm-conserving Vanderbilt (ONCV) pseudopotentials [49,50] and plane-wave (pw) basis; the other is a Fermi operator expansion (FOE) [51,52] approach using all-electron ONCV pseudopotentials. The PAWpw calculations are performed using the Vienna *Ab initio* Simulation Package (VASP) [53] and employing the hardest available PAW potentials (core radius equals 1.1 Bohr for both B and C), Perdew-Burke-Ernzerhof (PBE) [54] exchange-correlation functional, a large cutoff energy (2000 eV) for the pw basis, and the  $\Gamma$  point to sample the Brillouin zone. The PAWpw calculations of the EOS are performed at  $6.7 \times 10^3$ – $5.05 \times 10^5$  K ( $\sim 0.6$ – $43.5$  eV) and 1–10 times  $\rho_0$ . We conducted ONCVpw simulations [55] at temperatures up to  $3 \times 10^5$  K, using PBE exchange-correlation functional and a 900 eV energy cutoff (core radius equals 1.125 Bohr for both B and C) for the pw expansion, to cross-check the PAWpw results. For both PAWpw and ONCVpw calculations, a Nosé thermostat [56] is used to generate MD trajectories (typically  $\sim 5000$  steps) that form canonical ensembles. The MD time step is chosen within the range of 0.05–0.55 fs, smaller at higher temperatures. Cubic cells with 30 and 120 atoms are considered to eliminate the finite-size errors on the EOS.

We perform FOE calculations at temperatures of  $2.5 \times 10^5$ – $1.34 \times 10^6$  K. Note that FOE takes advantage of the smooth Fermi-Dirac function at high temperature by approximating the function with Chebychev polynomial expansion, which provides a very efficient way to conduct the Kohn-Sham DFT-MD calculation. We use 30-atom cells and conduct  $NVT$  simulations that last 3000–6000 steps (0.05–0.1 fs/step) to ensure sufficient statistics to obtain the EOS. To be consistent with the pw calculations, the FOE calculations employ PBE exchange-correlation functional and much larger energy cutoff (4000 eV) due to smaller core radius (0.8 Bohr) due to the inclusion of 1s core states in both B and C all-electron ONCV pseudopotentials. We also use the all-electron ONCV pseudopotentials and pw basis to perform calculations at densities of  $12.544$  g/cm<sup>3</sup> or higher and temperatures of  $1.26 \times 10^5$  K or lower, to reduce the possibility of frozen-core overlap in the MD simulations.

Over the last ten years, Militzer *et al.* have developed and employed the approach combining PIMC and DFT-MD to calculate the EOS of a series of elemental materials (He [57], B [13], C [42], N [58], O [59], Ne [58], Na [60,61], Mg [62], Al [63], Si [64]) and compounds (H<sub>2</sub>O [42], LiF [65], CH [46,47], BN [16], MgO [66], MgSiO<sub>3</sub> [67]) over wide ranges of temperatures and pressures. The PIMC data were shown to reproduce predictions by classical plasma theories (such as the Debye-Hückel and the ideal Fermi-gas model) in the limit of infinitely high temperatures and agree remarkably well (differences up to  $\sim 5\%$ ) with DFT-MD for the partially ionized, warm dense states at  $\sim 10^5$ – $10^6$  K (or 10–100 eV), while the DFT-MD predictions of the Hugoniot are consistent with dynamic shock experiments that are available up to multimegabar (Mbar) pressures. By fully capturing the ionic interaction effects (DFT-MD), nuclear quantum effects (PIMC), and electronic many-body effects (PIMC), these computations set accurate constraints for the EOS of these

materials ( $Z$  up to 14) from condensed matter to hot plasma states (degeneracy parameter  $\sim 0.1$ – $10^3$ , coupling parameter  $\sim 0.01$ – $10$ ) and serve as benchmarks for the development of other, computationally more efficient EOS methods.

In a recent paper [16], an all-electron, Green's function KKR electronic-structure method based on Kohn-Sham DFT and an activity expansion method, in addition to FOE and a spectral quadrature method, were used to compute the EOS of BN and compare with the PIMC and pw DFT-MD data. The Green's function method simplifies the calculation by using a static lattice and approximating the ion kinetic contribution with an ideal gas model, and show good agreement with PIMC and DFT-MD predictions at above  $10^5$  K when the ion thermal contribution becomes less significant in comparison to electron thermal or cold curve contributions. The activity expansion approach is based on an expansion of the plasma grand partition function in powers of the constituent particle activities (fugacities) [68,69], and the EOS calculations include interaction terms beyond the Debye-Hückel, electron-ion bound states and ion-core plasma polarization terms, along with relativistic and quantum corrections [70,71], and therefore produce accurate EOS at temperatures down to  $\sim 10^6$  K. It is thus interesting to explore the ranges of applicability of these approaches for  $B_4C$ .

We use the Multiple-scattering Electronic-structure Calculation for Complex Applications (MECCA) code for the all-electron, Green's function KKR calculations [72]. The KKR spherical-harmonic local basis included  $L_{\max} = 2$  within the multiple-scattering contributions, and  $L$  up to 200 are included automatically until the free-electron Bessel functions contribute zero to the single-site wave-function normalizations. We use local density approximation (LDA) [73] for the exchange-correlation functional, a  $12 \times 12 \times 12$  Monkhorst-Pack [74]  $k$ -point mesh for Brillouin zone integrations for energies with an imaginary part smaller than 0.25 Rydberg, and a  $8 \times 8 \times 8$   $k$ -point mesh otherwise. A denser mesh was used for the physical density of states calculated along the real-energy axes when needed. We use a static five-atom cubic cell for the calculations and approximate the ion-kinetic contribution by the ideal gas model. This structure can be equivalently viewed as a body-centered cubic carbon lattice that is centered at (0, 0, 0) and has a simple-cubic boron sublattice inscribed at  $(\pm 1/4, \pm 1/4, \pm 1/4)$ . This assumed crystal structure is by no means representative for  $B_4C$  at ambient conditions. Therefore, it is not expected to agree with experiments or other computational methods that do not assume this static structure. However, the structure is space filling and might be a representation for higher temperatures and pressures.

Activity expansion calculations are performed using the ACTEX code [68,69]. We cut off ACTEX calculations at temperatures below the point where many-body terms become comparable to the leading-order Saha term ( $T > 5.8 \times 10^5$  K).

### III. EXPERIMENTS

We present Hugoniot data for  $B_4C$  to 61 Mbar, exceeding the shock pressures achieved in previous experiments [36] by a factor of eight. The new data were obtained from

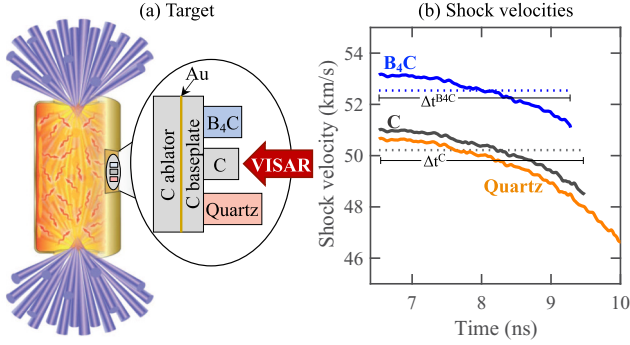


FIG. 2. (a) Target design and (b) shock velocities in the boron carbide ( $B_4C$ ), diamond (C), and quartz samples attached to the diamond baseplate for NIF shot N160414. Dotted lines in (b) show the average shock velocity in the samples determined from the measured thickness and shock transit time ( $\Delta t$ ). Solid curves show the time-dependent shock velocity histories, measured using VISAR for quartz (orange) and determined using the nonsteady waves correction for  $B_4C$  (blue) and diamond (gray).

experiments at the NIF [75], where the  $B_4C$  Hugoniot was measured relative to a diamond standard using the impedance-matching technique. The planar target package, which was affixed to the side of a laser-driven hohlraum, had a 200- $\mu\text{m}$ -thick diamond ablator, a gold preheat shield ranging in thickness from 2.9 to 10.9  $\mu\text{m}$ , a 100- $\mu\text{m}$ - or 125- $\mu\text{m}$ -thick diamond baseplate (the impedance-matching standard), and 140- to 166- $\mu\text{m}$ -thick  $B_4C$ , 134- to 148- $\mu\text{m}$ -thick diamond, and 285- $\mu\text{m}$ -thick quartz samples as shown in Fig. 2(a). The surfaces opposite the drive of the diamond baseplate and smaller diamond sample were flash coated with 100 nm of aluminum to facilitate shock break out time measurements. Densities of the polycrystalline diamond, z-cut  $\alpha$ -quartz, and  $B_4C$  were 3.515, 2.65, and 2.51  $\text{g}/\text{cm}^3$ , respectively [76]. The inner walls of the hohlraum were irradiated with 176 laser beams, which produced a  $\sim 200$  eV x-ray bath that drove a planar and nearly steady shock through the target package. The time-dependent shock velocity history in the quartz, measured using a line-imaging velocity interferometer system for any reflector (VISAR) [77], showed only  $\pm 3\%$  variation from the average over the relevant time period of the experiment. The

laser pulse duration, either 5 or 7.5 ns, and the total energy, between 519 and 820 kJ, varied shot-to-shot to produce high-pressure states in the  $B_4C$  spanning 27 to 61 Mbar.

The shock velocities in the diamond baseplate (standard) and  $B_4C$  sample at the material interface are required to determine the pressure-density state on the  $B_4C$  Hugoniot using the impedance-matching technique. The experimental  $B_4C$  Hugoniot data are given in Table I. Average shock velocities through the smaller diamond and  $B_4C$  samples were calculated from their thicknesses, measured using a dual confocal microscope, and the shock transit times, measured using VISAR. The *in situ* shock velocities in the  $B_4C$  and diamond samples were determined from the measured shock velocity history in the quartz using an analysis technique to correct for shock unsteadiness [78]. The average and *in situ* shock velocities are shown in Fig. 2(b).

In addition to the drive x rays, the interaction of the laser beams with the gold from the hohlraum wall produces high-energy x rays, which could preheat the EOS samples and thereby compromise the Hugoniot EOS measurement. The gold is not hot enough to produce K and L-shell radiation. The preheat shield between the ablator and the baseplate reduced the M-band x rays (2–15 keV) hitting the baseplate and the EOS samples to negligible levels. Besides a secondary effect, described in the next paragraph, we did not observe effects of preheat in the VISAR data due to either x rays or hot electrons.

A secondary preheat effect did occur for low pressure shots with 4.2  $\mu\text{m}$  gold layers (N170227 and N170503). This effect involved the heating and expansion of the preheat shield itself and the generation of an elastic compression wave through the baseplate into the samples ahead of the main shock wave. This effect was ameliorated in two ways. First, for the two shots in which it occurred, the matching velocity at the baseplate-sample interface was determined by extrapolating backwards from a time after the shock wave passed the preheat induced compression wave. In the second way, these shots were repeated with a thicker (10  $\mu\text{m}$ ) gold preheat layer and an altered laser pulse (N180411 and N180611). This reduced the compression wave strength and allowed the shock to overtake the wave within the baseplate, preventing precompression of the samples. The two sets of data reasonably agree, supporting our analysis method for the two affected shots.

TABLE I.  $B_4C$  Hugoniot data using the impedance-matching technique with a diamond standard. Shock velocities ( $U_s$ ) at the diamond standard/sample interfaces were measured *in situ* using VISAR for quartz (Q) and determined using the nonsteady waves correction for  $B_4C$  and diamond (C).  $U_s^C$  and  $U_s^{B_4C}$  were used in the impedance-matching analysis to determine the particle velocity ( $u_p$ ), pressure ( $P$ ), and density ( $\rho$ ) on the  $B_4C$  Hugoniot. The average shock velocities ( $\langle U_s \rangle$ ) determined from the measured thickness and shock transit times are also listed. The uncertainties for  $\langle U_s \rangle$  are the same as those given for  $U_s$ . The initial density of the  $B_4C$  samples was 2.51 ( $\pm 0.01$ )  $\text{g}/\text{cm}^3$ .

Shot #	$U_s^Q$ (km/s)	$\langle U_s^C \rangle$ (km/s)	$U_s^C$ (km/s)	$\langle U_s^{B_4C} \rangle$ (km/s)	$U_s^{B_4C}$ (km/s)	$u_p^{B_4C}$ (km/s)	$P^{B_4C}$ (Mbar)	$\rho^{B_4C}$ ( $\text{g}/\text{cm}^3$ )
N160414	50.65 $\pm$ 0.25	50.22	51.00 $\pm$ 0.35	52.54	53.15 $\pm$ 0.46	36.86 $\pm$ 0.39	49.38 $\pm$ 0.59	8.22 $\pm$ 0.29
N161002	56.57 $\pm$ 0.25	55.35	56.43 $\pm$ 0.50	57.43	58.63 $\pm$ 0.43	41.60 $\pm$ 0.55	61.46 $\pm$ 0.86	8.68 $\pm$ 0.35
N170227	44.30 $\pm$ 0.25	44.61	45.39 $\pm$ 0.33	46.77	47.62 $\pm$ 0.30	31.98 $\pm$ 0.36	38.38 $\pm$ 0.46	7.67 $\pm$ 0.22
N170503	38.17 $\pm$ 0.25	38.62	39.18 $\pm$ 0.29	39.65	40.38 $\pm$ 0.25	26.84 $\pm$ 0.31	27.31 $\pm$ 0.33	7.52 $\pm$ 0.21
N170808	51.22 $\pm$ 0.25	50.38	51.13 $\pm$ 0.41	53.22	54.04 $\pm$ 0.36	36.82 $\pm$ 0.45	50.15 $\pm$ 0.65	7.91 $\pm$ 0.25
N180411	43.98 $\pm$ 0.25	44.49	45.05 $\pm$ 0.37	46.56	47.15 $\pm$ 0.44	31.72 $\pm$ 0.40	37.67 $\pm$ 0.52	7.70 $\pm$ 0.28
N180611	39.67 $\pm$ 0.25	39.27	40.60 $\pm$ 0.40	40.68	42.15 $\pm$ 0.25	28.00 $\pm$ 0.43	29.74 $\pm$ 0.47	7.51 $\pm$ 0.26

The Hugoniot and release for the diamond standard were determined using LEOS 9061, a multiphase EOS for carbon based on DFT-MD and PIMC calculations [79]. Of the currently available diamond EOS tables, LEOS 9061 is the most consistent with recent experimental diamond Hugoniot data above 15 Mbar [80,81] and release data into quartz [80,82], which is applicable here because quartz is closely impedance-matched to B<sub>4</sub>C. We acknowledge that the diamond EOS is not yet experimentally calibrated above ~27 Mbar at the pressures in our experiments, leading to systematic uncertainties in our analysis. Further details on the experimental configuration, systematics of the diamond EOS, and analysis techniques, including a detailed discussion of precursor effect and mitigation in the analysis can be found in Ref. [83], which reports on quartz and molybdenum data that were acquired simultaneously with the B<sub>4</sub>C data presented here. We estimate that the reanalysis of the B<sub>4</sub>C data using other diamond EOS models is within the error of our results (~4% in density), based on the systematics study of the simultaneously acquired quartz results that was done in Sec. VI C of Ref. [83].

## IV. RESULTS AND DISCUSSION

### A. Hugoniot comparison

In this section, we compare our experimental measurements of the pressure-density Hugoniot of B<sub>4</sub>C with our theoretical predictions. The theoretical Hugoniot curves are obtained by fitting the EOS along each isotherm or isochore using cubic splines and then finding the pressure, density, and temperature that satisfy the Rankine-Hugoniot equation  $E - E_i + (P + P_i)(V - V_i)/2.0 = 0$ , where  $(E, P, V)$  denote the internal energy, pressure, and volume of B<sub>4</sub>C under shock and  $(E_i, P_i, V_i)$  are the corresponding values at the initial state. For PAWpw (similar for all the ONCV calculations),  $E_i$  and  $P_i$  are approximated by running DFT calculations for a 45-atom trigonal structure [84] of B<sub>4</sub>C at the density of interest ( $\rho_i = 2.51$  g/cm<sup>3</sup>); the same values are used for PIMC after an energy shift ( $-136.1308$  Ha/B<sub>4</sub>C, determined by all-electron calculations for isolated B and C atoms using the OPIUM code [85] and the PBE exchange-correlation functional) that aligns PAWpw with the all-electron PIMC EOS; for MECCA, we use the values for  $E_i$  and  $P_i$  that are calculated at 300 K and  $\rho_i$  using the same five-atom structure as that for producing the EOS data; for ACTEX, we use 1 atmosphere pressure for  $P_i$  and the cohesive energy of B<sub>4</sub>C from Ref. [86] (7.17 eV/atom), and confirmed that a  $\pm 20\%$  change in  $E_i$  does not influence the calculated Hugoniot.

Figure 3 compiles the experimental and theoretical Hugoniot curves in pressure-density and temperature-density plots. The comparison shows very good consistency between the measurements and the theoretical predictions. Assisted by the theoretical predictions, we estimate Hugoniot temperatures for the experimental data to be in the range of  $1\text{--}5 \times 10^5$  K. Our results also show that the PIMC and DFT-MD predicted Hugoniot are in overall good consistency with LEOS 2122 (L2122). Our calculations and the L2122 model predicts B<sub>4</sub>C to have a maximum compression ratio of 4.55 at  $9 \times 10^2$  Mbar and  $2 \times 10^6$  K, below which L2122 predicts B<sub>4</sub>C to be slightly softer. We also note that the pressure-density Hugo-

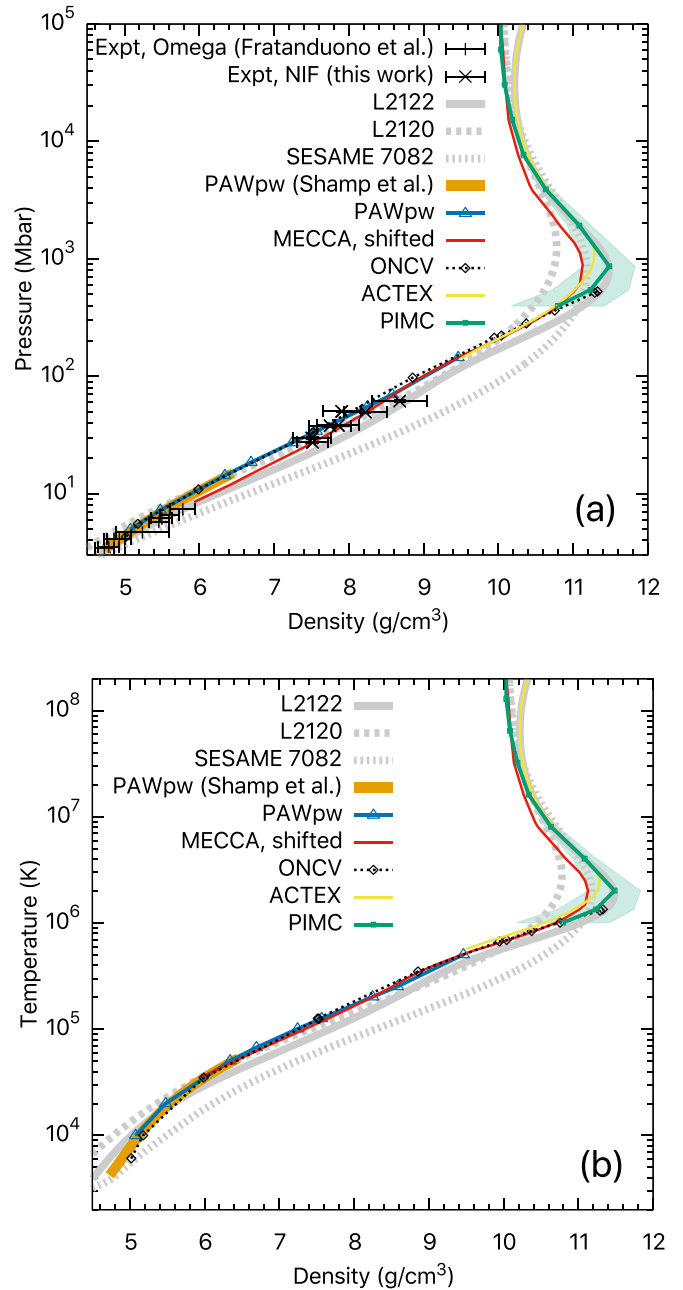


FIG. 3. Comparison of the Hugoniot of B<sub>4</sub>C predicted by various simulations and the LEOS/SESAME models in (a) pressure-density and (b) temperature-density representations. Also shown in (a) is our experimental data collected at the NIF and those by Fratanduono *et al.* [36] at Omega laser facility. The shaded areas around the lower end of the PIMC curve represent  $1\sigma$  uncertainty in the corresponding Hugoniot density due to EOS errors. All pressures in our MECCA EOS table have been shifted up by 97.1 GPa, so that the value at ambient is zero. ONCV denotes the Hugoniot curve from ONCV pseudopotential calculations that involve pseudopotentials with or without 1s core states and use either pw or FOE method (see Figs. 1 and 5 for the temperature-density regions at which pw and FOE methods are used). The deviation between PIMC/L2120 (and MECCA) and ACTEX/L2122 curves above  $10^4$  Mbar is due to the electron relativistic effect, which is considered in ACTEX and L2122 but not in PIMC/L2120 (and not fully in MECCA). The initial sample density  $\rho_i = 2.51$  g/cm<sup>3</sup> for all the Hugoniot except that by Shamp *et al.* [37], which is 2.529 g/cm<sup>3</sup>.

niots predicted by a different Thomas-Fermi-based tabular model L2120 is very similar at pressure ranges other than that around the compression maximum, at which the L2120 prediction is stiffer by  $\sim 6\%$ . This can be attributed to the K-shell ionization that is fully captured by our calculations and the Purgatorio model L2122, while no atomic shell effects has been included in Thomas-Fermi models. In comparison, another Thomas-Fermi table (SESAME 7082), although reasonably agreeing with the low-pressure OMEGA data, can be clearly ruled out by our NIF data and computations. This may be attributed to the inaccuracies in the cold curve and the ion thermal model used in the table. The latest NIF gigabar (Gbar) experiments obtain Hugoniot of CH and B near the compression maxima that agree with our PIMC calculations better than Thomas-Fermi predictions [87,88]. We expect future, accurate experiments at Gbar pressures to test our predictions for  $B_4C$ .

At 3–400 Mbar and  $10^4$ – $10^6$  K, the Hugoniot curve obtained from MECCA and those from DFT-MD (PAWpw, ONCVpw, and ONCV-FOE) agree remarkably well with each other. Because MECCA calculations are based on a static lattice and the ion thermal contribution to the EOS is added following an ideal gas model, the good consistency implies that the ion thermal contribution is dominated by the ion kinetic effect. We note that ACTEX predictions of the Hugoniot down to  $6 \times 10^5$  K and 140 Mbar also agree very well with the DFT predictions.

The computational predictions are consistent with the NIF experimental data at pressures above 27 Mbar, as well as those conducted at the Omega laser facility [36] up to 5 Mbar. However, at 5–10 Mbar, the experimental Hugoniot seems to be softer than DFT-MD predictions, similar to findings by a previous DFT-MD study that was performed up to 15 Mbar [37], which might be attributed to chemical separation of the  $B_4C$  samples as has been carefully explored for solid  $B_4C$  at low temperatures in Ref. [37].

We note that, at temperatures of  $1$ – $4 \times 10^6$  K, our PIMC data for  $B_4C$  have large errors (up to  $\sim 2\%$ ) because of the large computational cost and stochastic noise at these conditions. The error quickly drops down with increasing temperature. We use a Monte Carlo approach to estimate the associated uncertainty in density along the Hugoniot by taking into account the errors in the PIMC data. The results are shown with the green shaded area in Fig. 3. It is clear that the PIMC Hugoniot is in excellent agreement with L2122 predictions and is consistent with those predicted by ACTEX and MECCA within the error bar. Slight differences of up to 2–3% can be observed at 400–10,000 Mbar and  $10^6$ – $10^7$  K. This may be due to different approximations between ACTEX/MECCA and PIMC/Purgatorio.

To better understand the origin of the differences at the compression maximum, we compare the energy [ $E - E_i$ ] and the pressure [ $(P + P_i)(V_i - V)/2.0$ ] terms of the Hugoniot function from PIMC, ACTEX, MECCA, and LEOS 2122 along two isotherms ( $1.3 \times 10^6$  K and  $2 \times 10^6$  K, see Fig. 4). The cross point between the curve of the energy term and that of the pressure term gives the Hugoniot density at the corresponding temperature. Our comparison shows that the internal energy slowly decreases while the pressure term dramatically increases, as the density increases from 9 to  $14 \text{ g/cm}^3$ .

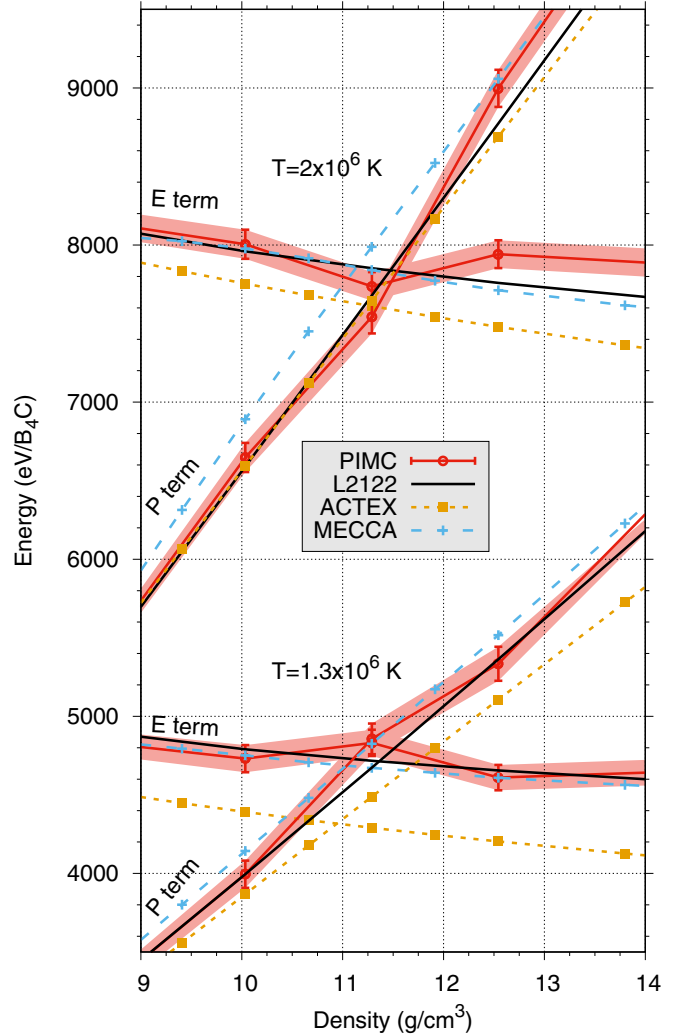


FIG. 4. Comparison of the energy and pressure terms (in units of eV per formula unit of  $B_4C$ ) of the Hugoniot function from different theories and LEOS models at two temperatures around the compression maximum. The shaded area denote the standard error of the PIMC EOS. Note that the shift (97.1 GPa) applied to MECCA pressures is negligible in comparison to the absolute values of the pressure (400–1100 Mbar) at the conditions shown here.

Due to the high computational expense of PIMC simulations at low-temperature conditions, our PIMC data at low temperatures exhibit significantly larger error bars and stochastic noise than the higher temperature results. The error bars of the PIMC data lead to estimations of the  $1\sigma$  uncertainty in Hugoniot density, as is shown with shaded green areas in Fig. 3. L2122 and PIMC agree well with each other in both energy and pressure, explaining the excellent consistency between their predicted Hugoniot. MECCA shifted pressures are slightly higher than PIMC, whereas energies are similar, therefore the Hugoniot density is also lower. In comparison to PIMC, ACTEX energies are lower, while pressures are similar at  $1.3 \times 10^6$  K but lower at  $2 \times 10^6$  K, therefore the Hugoniot densities from ACTEX are also lower.

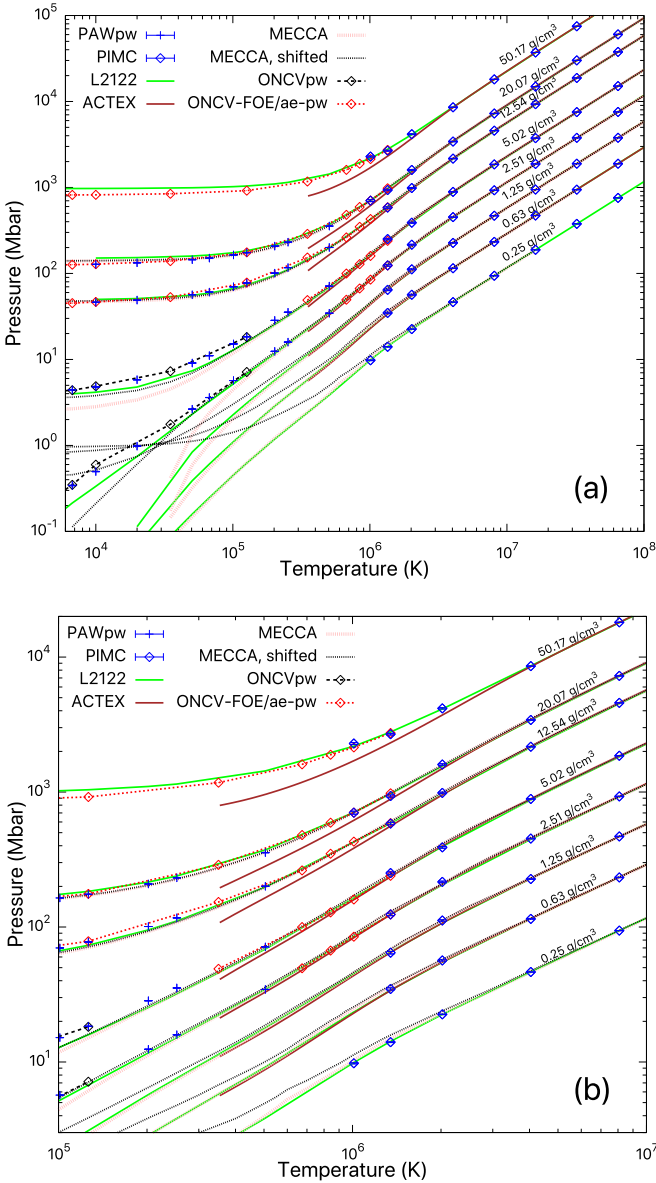


FIG. 5. Comparison of the pressure-temperature profiles of  $B_4C$  along several isochores from PIMC, DFT-MD [PAWpw, frozen 1s; ONCVpw, frozen 1s; ONCV-FOE or ae-pw, all-electron], ACTEX, MECCA, and L2122. Also included is a set of MECCA data that have been shifted up by 97.1 GPa, so that the value at ambient is zero. Subplot (b) is a zoom-in version of (a).

### B. EOS comparison

The principal Hugoniot samples a specific path in the phase space from 2.5 to 11.5  $g/cm^3$  accompanied by increasing temperatures. These conditions are very important because the corresponding states are reachable using shock experiments. However, off-Hugoniot states, as those simulated in the present work, also play vital roles in hydrodynamic simulations and the underlying physics can be different. We therefore make detailed comparisons of the EOS [89] among various methods in this subsection.

The pressure-temperature data along several isochores from our calculations are compared in Fig. 5. At  $4 \times 10^6$  K

and above, all our methods (PIMC, ACTEX, and MECCA) agree and are consistent with the L2122 model. This is understandable because the system is approaching the limit of a fully ionized classical plasma, which is accurately described by PIMC, ACTEX, and the DFT methods MECCA and Purgatorio.

At lower temperatures, the different ways of employing DFT-MD (PAWpw, ONCVpw, and ONCV-FOE) give the same EOS and consistent trend with the PIMC data. Several differences are noteworthy when other methods (ACTEX, MECCA, and L2122) are considered: (1) ACTEX pressures being lower than others, more so at higher densities; (2) MECCA pressures being significantly different from L2122 at 5  $g/cm^3$  and below, in particular at  $T < 10^5$  K; (3) with a constant shift of +97.1 GPa (so that the ambient pressure is zero), MECCA pressures agree better with L2122 at ambient density and above, but worse at lower-than-ambient densities; and (4) all-electron ONCV pressures gets slightly lower than L2122 for densities higher than 25  $g/cm^3$ .

Figure 6 focuses on the differences between the first-principles PIMC/DFT-MD data and L2122  $\Delta P = (P^{FP} - P^{L2122})/P^{L2122} \times 100\%$ . The agreement is well within 3% for all densities studied presently and temperatures above  $4 \times 10^6$  K. At lower temperatures,  $\Delta P$  varies between  $\pm 17\%$  depending on the density—DFT-MD pressures are in general higher at densities below 10  $g/cm^3$  and lower above.  $|\Delta P|$  becomes smaller than 10% and gradually vanishes when temperature increases to  $3.5 \times 10^5$  K or above. PAWpw and ONCVpw/ONCV-FOE predictions are overall the same. ONCV-FOE smoothly bridges with PIMC predictions at  $10^6$  K.

We also compare the pressures and energies from our different computations with those from L2122. The results along two isotherms  $1.3 \times 10^6$  and  $2 \times 10^6$  K are shown in Fig. 7. We find that PIMC, MECCA, and ONCV-FOE agree with each other to within 5%, which is comparable to what we found about differences between PIMC and DFT-MD in previous work on B [13], BN [16], and hydrocarbon systems [46,47]. The cross validation of the different DFT methods and their consistency with PIMC predictions confirm that both the PIMC and the DFT-MD approaches, albeit carrying approximations in each, are reliable for studying the EOS of warm dense matter. Our ACTEX data also show remarkable consistency (e.g.,  $< 2\%$  at  $2 \times 10^6$  K) with L2122 at densities below 10  $g/cm^3$ . However, the ACTEX pressure and internal energy get way too low at higher densities, which is due to breakdown of the ACTEX method when the two-body term at order 2 in the activity becomes comparable to the Saha term, similar to what has been found for BN [16].

### C. Modifications to L2122 and 1D hydrodynamic simulations

We have shown in Fig. 3 that L2122 predicts slightly softer behavior for  $B_4C$  at 5–500 Mbar, despite the overall good consistency, in comparison with our first-principles and experimental Hugoniot. We have thus created three new models for the  $B_4C$  EOS, with the intent to span the range of Hugoniot behavior that is in better agreement with the experimental data from both NIF and Omega. Recent advances in ICF design methodologies that leverage Bayesian inference

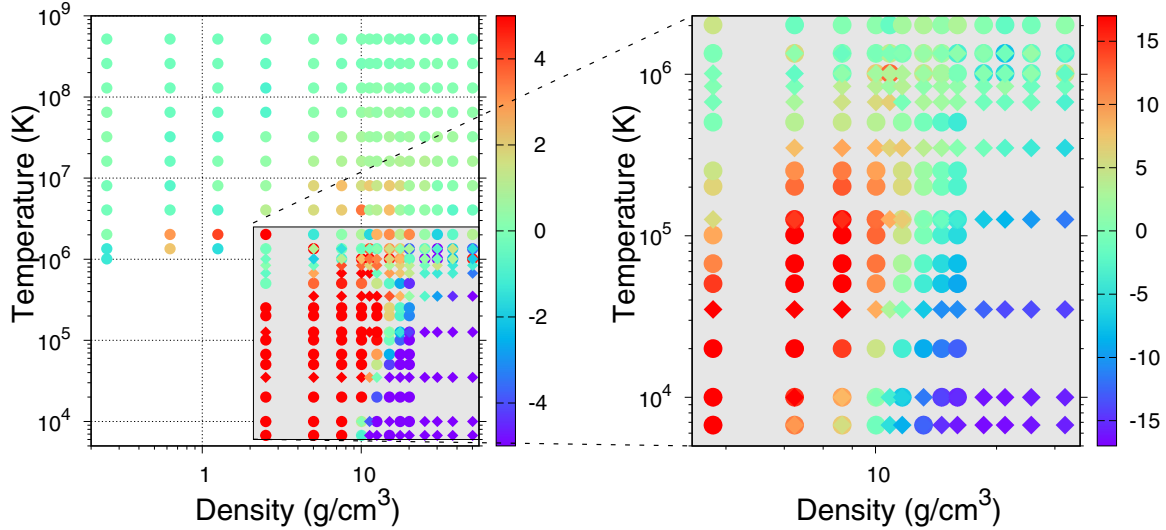


FIG. 6. Percent difference in pressure of  $B_4C$  between PIMC/PAWpw (in spheres) or ONCV (in diamonds) and L2122.

techniques to find most probable physics models based on a range of experimental outcomes [90] and recent interest in  $B_4C$  as an ablator for such experiments motivated us to create this range of possible EOS models rather than just a single table. By considering the range of reasonable EOS models for  $B_4C$  as obtained from our above comparisons of theoretical methods and experimental uncertainty, we developed these three new tables by making modifications to the cold curve and the Grüneisen parameter within the QEOS methodology.

The Hugoniot curves corresponding to the new models (L2123, L2124, and L2125) are shown in Fig. 8, along with the experimental data. The PIMC Hugoniot with error bars is also shown. The new baseline model (L2123) has a slight modification to the cold curve, and to the Grüneisen parameter, which determines the ion thermal EOS, to bring it into better agreement with both sets of experimental data. L2124 and L2125 have modified forms of the cold curve that span the range of the experimental error bars. Both L2123 and L2124 (the softer model) closely track L2122 near peak compression, whereas the L2125 (the stiffer model) shows significantly modified behavior near peak compression.

We applied these new models to 1D hydrodynamic simulations of a polar direct drive fusion experiment based on previous studies [19,91]. For this study, we kept the capsule diameter constant at  $3000 \mu\text{m}$  and set the gas pressure to 8 atm of  $D_2$  at room temperature. We used a flux limiter = 0.0398 and a square pulse shape with peak power set to 280 TW. The pulse duration was chosen such that 476 kJ of energy would be available from the laser. Due to geometric losses, we assumed that the maximum absorption of energy would correspond to 75% of the total energy available. Similar to our previous work on boron [13], we found that the EOS variations we considered here did not produce significant differences in the fuel areal density, peak ion temperature, or ablator areal density in these direct drive simulations.

To expand this sensitivity study to situations that might be more relevant to future neutron source development studies [92], we also examined the neutron yield versus ablator thick-

ness for each of the three EOS models. Interestingly, all four EOS models (L2122–L2125) predict similar profiles for the neutron yield with a peak yield that occurs around an ablator thickness of  $7.5 \mu\text{m}$ . Differences between the models are all within 1% for thin ( $< 10 \mu\text{m}$ ) ablators. For ablator thickness between  $10\text{--}25 \mu\text{m}$ , we found the neutron yield from L2123 remains similar ( $< 0.2\%$ ), while that from L2124 and L2125 deviate by up to 3%, in comparison to L2122. These results demonstrate the availability of these models for use in future studies in ICF design with novel ablators.

## V. DISCUSSION

For the sake of benefiting future EOS development, high-energy density physics, and warm dense matter studies, we hereafter discuss the physical origins of the EOS differences shown above from electronic-structure and QEOS points of view.

### A. Finite-size effects

Our first-principles calculations PIMC, PAWpw, ONCVpw, and ONCV-FOE implement the standard way of simulating liquids [93], which considers a finite number of atoms in a cubic box and under the periodic boundary condition. The finite-cell size effects have been carefully addressed in our DFT-MD simulations by choosing large-enough cells with 120 atoms for all temperatures up to  $2.5 \times 10^5 \text{ K}$  ( $\sim 20 \text{ eV}$ ). This is much higher than the chemical bonding is allowed (typically about a few eV), which justifies the use of 30-atom cells for all simulations at higher temperatures. To show this, Fig. 9 compares the nuclear pair correlation function at two different temperatures ( $10^4$  and  $10^5 \text{ K}$ ) and two different densities ( $2.5$  and  $12.5 \text{ g/cm}^3$ ) using two different cells sizes (30 and 120 atoms), from our PAWpw calculations. The results show remarkably good agreement in the features of  $g(r)$  using 30-atom cells with those using the much larger 120-atom cells even at the relatively low-temperature ( $10^4 \text{ K}$ ), high-density ( $12.5 \text{ g/cm}^3$ ) condition. This is different from



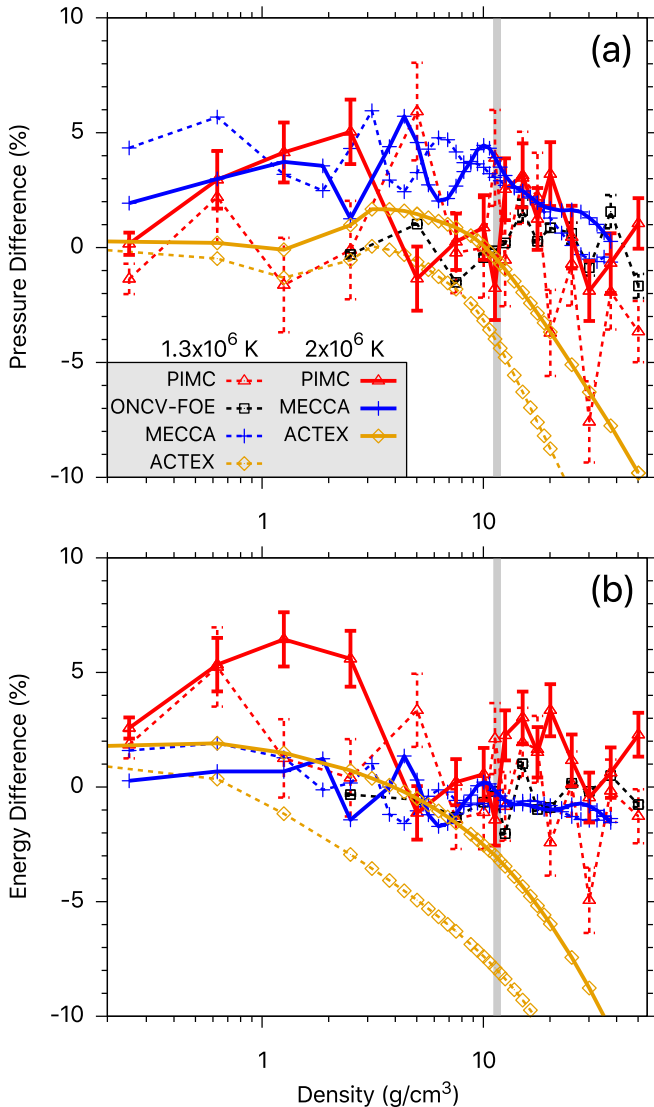


FIG. 7. EOS differences of PIMC (red), ONCV-FOE (black), MECCA (blue), and ACTEX (yellow) relative to LEOS 2122 along two isotherms [ $1.3 \times 10^6$  (dashed curves) and  $2.0 \times 10^6$  K (solid curves)]. Because of the different references chosen in the EOS datasets, all energies have been shifted by the corresponding values at ambient condition ( $2.5087 \text{ g/cm}^3$  and  $300 \text{ K}$ , same as the initial energy for the Hugoniot computations as described in Sec. IV A). The pressure differences are normalized by the corresponding LEOS 2122 values; the energy differences are normalized by the ideal nuclei-electron gas values ( $46.5k_B T$  per  $\text{B}_4\text{C}$ ). The statistical error bars correspond to the  $1\sigma$  uncertainty of the FOE and PIMC data. The gray vertical bar at  $11.54 \text{ g/cm}^3$  denotes the maximum Hugoniot density according to LEOS 2122 and PIMC.

our recent findings for BN, which show stronger size dependence at similar conditions, and is probably due to larger polarization effects (associated with the larger difference in electronegativity between B and N than between B and C) in BN than in  $\text{B}_4\text{C}$ . Moreover, peak-valley structures can be clearly seen in the pair correlation plot at  $10^4 \text{ K}$ , which are signatures of atomic clustering and chemical bonding. Note that the bonding is likely very short lived, because of the high temperatures [47]. At  $10^5 \text{ K}$ , these structures smooth out and

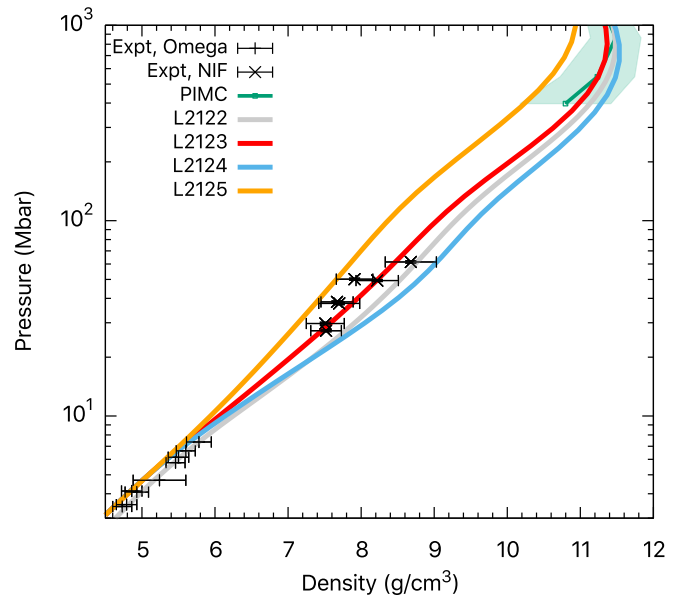


FIG. 8. Comparison of the Hugoniot ( $\rho_i=2.51 \text{ g/cm}^3$ ) of  $\text{B}_4\text{C}$  from newly constructed QEOS models (L2123, L2124, and L2125) and those from experiments, PIMC simulations, and L2122.

the  $g(r)$  becomes more ideal-gas like, which validates the ideal mixing approximation in multicomponent average-atom EOS approaches [46,47].

At temperatures below  $10^5 \text{ K}$ , chemical bonding has to be described using reasonably big simulation cells so that the EOS can be accurately obtained. In Sec. IV B, we show that MECCA calculations using a five-atom cell produce a pressure ( $-97.1 \text{ GPa}$ ) that is significantly different from  $1 \text{ bar}$

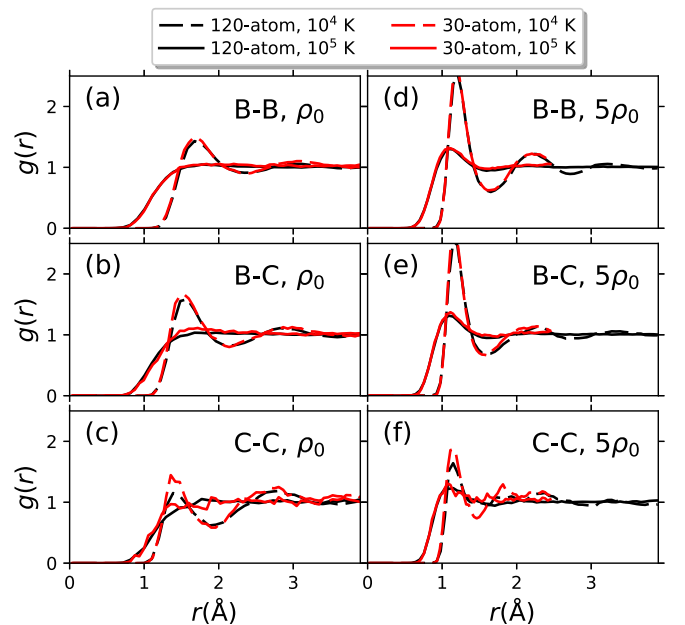


FIG. 9. Comparison of the nuclear pair correlation function obtained from DFT-MD (PAWpw) for  $\text{B}_4\text{C}$  using 30-atom (red) and 120-atom (dark) cells at two different densities and two temperatures. The reference density  $\rho_0$  is  $2.5087 \text{ g/cm}^3$ .

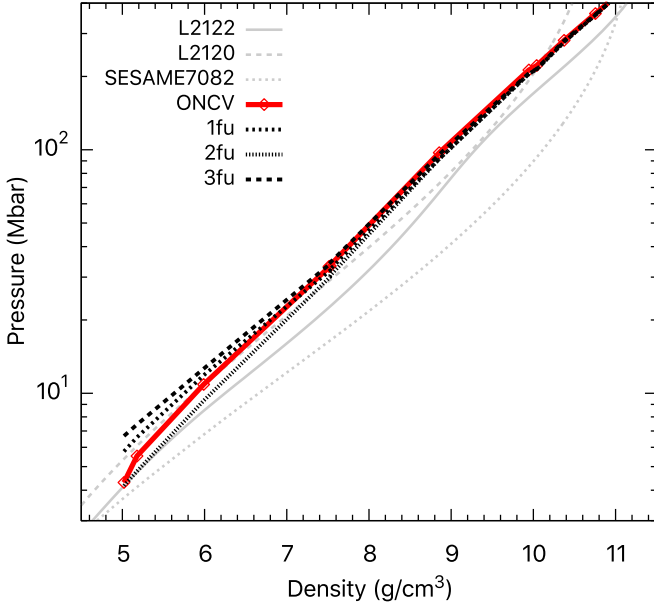


FIG. 10. Comparison of pressures from single-snapshot calculations using various cells [1 formula unit (fu): 5-atom cell; 2 fu: 10-atom cell; 3 fu: 15-atom cell] at the ONCV Hugoniot densities and temperatures (see Fig. 3). The Hugoniot from three EOS models are also shown for comparison.

at ambient condition, and therefore a rigid shift in pressure for the MECCA EOS table has to be applied to improve the agreement between MECCA and DFT-MD Hugoniot. It is worthwhile to investigate the effect of using such small sizes in more depth by making comparisons with slightly larger ones.

We constructed three structures consisting of 5, 10, and 15 atoms, respectively [94], and performed additional pw-based single-snapshot calculations using all-electron ONCV pseudopotentials along the density-temperature Hugoniot predicted using the ONCVpw/ONCV-FOE EOS. The pressure data as a function of density from the new ONCV calculations are compared in Fig. 10. The results show that using 10-atom cells brings the pressure down relative to that using 5-atom cells. However, using larger, 15-atom cells leads pressure to the opposite direction, instead of approaching the converged values. The differences as signatures of ion thermal and cold-curve effects on the EOS of  $B_4C$  are observable along the Hugoniot at densities up to  $9 \text{ g/cm}^3$ , which is  $\sim 100 \text{ Mbar}$  and  $\sim 3 \times 10^5 \text{ K}$ .

### B. Roles of kinetic and interaction contributions from ions and electrons

To clarify the roles of kinetic and interaction contributions from the ions and from the electrons, we performed additional analysis of our pw-based all-electron ONCV calculations. The calculations allow decomposing the total pressure into an ion-kinetic (IK) term, which is calculated using the ideal gas model, and a remaining term (P-IK) (Fig. 11). In comparison to the QEOS way of decomposing the L2122 Hugoniot pressure into ion-thermal, electron-thermal, and cold curve

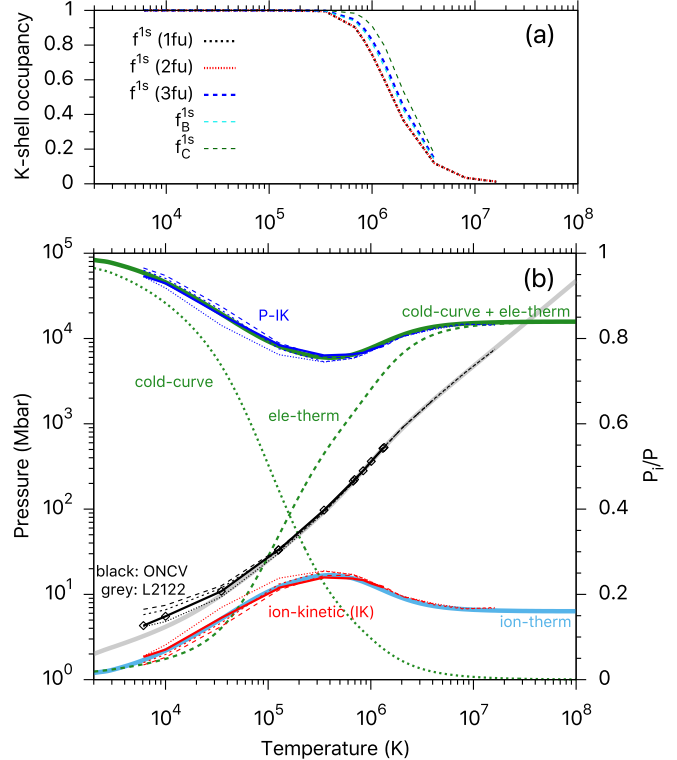


FIG. 11. (a) K-shell occupancy of boron and carbon atoms and the average values as obtained from ONCV calculations using different cell sizes [short dashed: 1 formula unit (fu) (5-atom cell); dotted: 2 fu (10-atom cell); dashed: 3 fu (15-atom cell)]. (b) Fractional decomposition of pressure (colored curves, right axis) in the LEOS 2122 model and ONCV calculations along their respective Hugoniot (black/grey curves, left axis). In (b), the pressures calculated at the ONCV Hugoniot temperature and density conditions [see Fig. 3(b)] using smaller cells are shown for comparison.

components, we find that the IK contribution is overlapping with the ion-thermal term in L2122.

In addition, we find that the temperatures at which finite cell size effects are significant, as characterized by the differences between solid and dashed curves, overlap with those at which the cold-curve surpasses the ion-thermal contributions. The turn-over point  $T_t$ ,  $\sim 3 \times 10^5 \text{ K}$  for  $B_4C$ , may be interpreted as a conservative estimation of the uppermost temperature at which finite-size effect remains significant in a theoretical computation, or the lowermost temperature at which an average-atom approach is feasible. Below  $T_t$ , interactions are so significant that the ideal mixing approximation becomes less reliable and a large simulation cell is required for the accuracy of computations.

As temperature increases to a critical value  $T_c$  where K-shell ionization starts, the electron-thermal contribution becomes dominant. This leads to a saddle point in the IK and the P-IK curves in Fig. 11. Our present calculations show  $T_c = 3 \times 10^5 \text{ K}$  for  $B_4C$ , which is close to what we previously obtained for pure boron [13] and slightly below that for carbon. This is not unexpected because the K level is deeper for elements with higher  $Z$ . At temperatures above  $\sim 2 \times 10^7 \text{ K}$ ,  $B_4C$  is fully ionized and the EOS is dominated

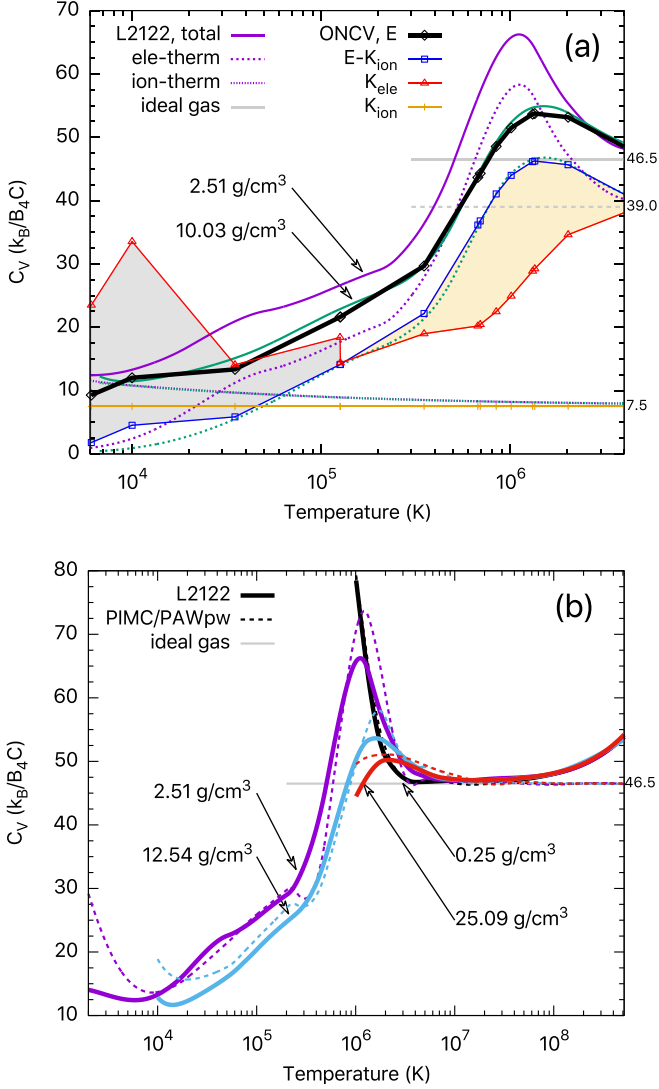


FIG. 12. (a) Decomposition of the heat capacity from LEOS 2122 along two isochores and ONCV along the Hugoniot. (b) Heat capacity comparison between LEOS 2122 and PIMC/PAWpw along four isochores in a broader range of temperatures than that shown in (a). In (a), LEOS 2122 results (purple and green curves) are decomposed into electron-thermal (short dashed) and ion-thermal (thick dotted) terms. ONCV data (dark line-points) are decomposed into ion kinetic (yellow), electron kinetic (red), and interaction (i.e., the difference between the all-except-ion kinetic, in blue, and electron kinetic) terms.

by the ideal gas-like contributions from the nuclei and the electrons.

To further elucidate the roles of interaction and kinetics in the EOS, we calculate their respective contributions to the heat capacity  $C_V$  along the Hugoniot using the all-electron ONCV pseudopotentials, and the results are shown in Fig. 12(a). The ion kinetic term ( $K_{\text{ion}}$ ) contributes  $7.5 k_B/B_4C$  to  $C_V$  independent of temperature, where  $k_B$  is the Boltzmann constant. Electron kinetic contributions ( $K_{\text{ele}}$ ) are generally higher (above  $15k_B/B_4C$ ) and show two bumps, one at  $10^4$  K and the other at  $10^6$  K, which can be attributed to the L- and the K-shell ionization, respectively. In contrast to  $K_{\text{ion}}$  which fol-

lows an ideal gas model at all temperatures,  $K_{\text{ele}}$  is dependent on both the electronic orbitals and their occupancy, instead of purely on ionization, and is not ideal gas-like until the system is fully ionized. This can be seen from its asymptotically approaching the ideal electron gas value of  $39k_B/B_4C$  at above  $4 \times 10^6$  K.

The interaction effects on the EOS are more complicated and consist of contributions by ion-ion (“Ewald”), electron-ion (“external”), and electron-electron (“exchange-correlation” and “Hartree”) interactions. For simplicity of EOS discussions, it might be easier to group them together than to present individually. This is clearly shown by the difference between the red ( $K_{\text{ele}}$ ) and the blue ( $E - K_{\text{ion}}$ , meaning all except ion kinetic contributions) line-points in Fig. 12(a). The net effect of interactions can be categorized into two regions: I (gray shaded) is below  $\sim 10^5$  K with  $K_{\text{ele}} > E - K_{\text{ion}}$  and implying negative net contribution of interaction to  $C_V$ ; II (yellow shaded) is above  $\sim 10^5$  K with  $K_{\text{ele}} < E - K_{\text{ion}}$  implying positive contributions of interaction to  $C_V$ .

At  $\sim 6 \times 10^3$  K,  $K_{\text{ele}}$  contributions are largely offset by electron-electron and ion-ion repulsion, therefore  $C_V$  is dominated by  $K_{\text{ion}}$ . As temperature increases, the repulsive contribution is gradually offset by the electron-ion attraction, therefore the net interaction contribution gradually increases to zero at  $\sim 1.5 \times 10^5$  K and becomes positive at higher temperatures where K-shell ionization occurs. As the system becomes fully ionized at above  $4 \times 10^6$  K,  $K_{\text{ele}}$  and  $K_{\text{ion}}$  contributions dominate.

Figure 12(a) also compares  $C_V$  along two isochores [ $2.51 \text{ g/cm}^3$  (purple) and  $10.03 \text{ g/cm}^3$  (green)] from L2122, which approximately encapsulate the Hugoniot at the temperatures being shown. As a QEOS model, L2122 decomposes the free energy into three terms: cold-curve, ion-thermal, and electron-thermal. The ion-thermal term (dotted lines) includes both kinetic and interaction effects such as those from vibration. This explains their differences relative to the  $K_{\text{ion}}$  curves, as well as the consistency between the electron thermal (dashed lines) and  $E - K_{\text{ion}}$  (blue line-points), because the cold curve does not contribute to  $C_V$ . We also note [Fig. 12(b)] that the  $C_V$  curves [along four isochores:  $0.25 \text{ g/cm}^3$  (black),  $2.51 \text{ g/cm}^3$  (purple),  $12.54 \text{ g/cm}^3$  (blue), and  $25.09 \text{ g/cm}^3$  (red)] from our PIMC/PAWpw calculations in the broad temperature range are consistent with L2122 predictions, except for temperatures above  $2 \times 10^7$  K, because the electron relativistic effect that is included in the L2122 model raises the internal energy and heat capacity and shifts the Hugoniot toward the limit of seven times compression at infinitely high temperature.

## VI. CONCLUSIONS

In this work, we present a comprehensive study of the EOS of  $B_4C$  over a wide range of pressures and temperatures by implementing several computational methods, including PIMC, DFT-MD using standard plane-wave basis and PAW or ONCV pseudopotentials, ACTEX, and MECCA.

Our EOS data by PIMC, FOE, ACTEX, and MECCA show good consistency at  $10^6$  K where 1s electrons are ionized. Our detailed EOS comparison provides strong evidences that cross

validate both the PIMC and the DFT-MD approaches for EOS studies of the partially ionized, warm-dense plasmas.

At  $2.5\text{--}3.2 \times 10^6$  K and  $1.0\text{--}1.3 \times 10^3$  Mbar, our PIMC, AC-TEX, and MECCA calculations uniformly predict a maximum compression of  $\sim 4.55$  along the shock Hugoniot for  $\text{B}_4\text{C}$  ( $\rho_i = 2.51$  g/cm<sup>3</sup>), which originates from K shell ionization. This compression is underestimated by Thomas-Fermi models by  $\sim 0.2$  (6%). The maximum compression ratio is similar to that of h-BN ( $4.55$  for  $\rho_i = 2.26$  g/cm<sup>3</sup>) [16] and slightly smaller than pure boron ( $4.58$  for  $\rho_i = 2.31$  g/cm<sup>3</sup>) [13].

We also report Hugoniot data up to  $\sim 61$  Mbar from experiments at the NIF. The measured data show good agreement with our theoretical predictions based on DFT-MD.

By comparing QEOS models with the electron thermal term constructed in different ways (Purgatorio in LEOS 2122 or Thomas-Fermi in LEOS 2120/SESAME 7082), we find that the Purgatorio-based EOS models provide excellent overall agreement with our numerical simulations, similar to our previous studies on pure boron and BN. Because the largest differences in the Hugoniot response of the models occurs near peak compression, performing experiments for materials near peak compression [3,4,95–97] would provide a rigorous experimental test of our understanding of electronic structure in high-energy density plasmas. It would also be worthwhile to pursue experiments that provide measurements of the temperature and the pressure in either Hugoniot or off-Hugoniot experiments, which would provide data to test the first-principles calculations.

Based on the experimental data, we have developed three new EOS models (L2123, L2124, and L2125) by variations of the cold curve and the ion thermal EOS model to span the range of experimental error bars. To test the applicability of the models to simulations of ICF, we performed a series of 1D hydrodynamic simulations of direct drive implosions with a  $\text{B}_4\text{C}$  ablator based on the polar direct drive exploding pusher platform described in Refs. [19,91,92]. Because the yield in these implosions of relatively thin capsules is strongly dominated by the shock heating of the gas and not reliant on very high compression of the ablator, the most relevant part in the phase space for these implosions is predominantly

the shock generation along the principal Hugoniot. We find that the nominal polar direct drive exploding pusher design with a 1.8 ns, 500 kJ square laser pulse is not sensitive to the choice of these four EOS models (including L2122) for capsule thicknesses ranging from 2 to 25  $\mu\text{m}$ . The thickest shells considered showed significantly higher densities (up to  $\sim 45$  g/cm<sup>3</sup>) than thinner shells at stagnation, yet the computed yield was still insensitive to the level of EOS variation that is represented by the models we have developed. Our work should motivate similar studies for future indirect and direct drive ICF designs using  $\text{B}_4\text{C}$  ablators.

## ACKNOWLEDGMENTS

This work was in part performed under the auspices of the U.S. Department of Energy by Lawrence Livermore National Laboratory under Contract No. DE-AC52-07NA27344. Computational support was provided by LLNL high-performance computing facility (Quartz) and the Blue Waters sustained-petascale computing project (No. NSF ACI 1640776). B.M. is supported by the U.S. Department of Energy (Grant No. DE-SC0016248) and the University of California. S.Z. was partially supported by the PLS-Postdoctoral Grant of LLNL.

This document was prepared as an account of work sponsored by an agency of the United States government. Neither the United States government nor any agency thereof, nor any of their employees, makes any warranty, express or implied, or assumes any legal liability or responsibility for the accuracy, completeness, or usefulness of any information, apparatus, product, or process disclosed, or represents that its use would not infringe privately owned rights. Reference herein to any specific commercial product, process, or service by trade name, trademark, manufacturer, or otherwise does not necessarily constitute or imply its endorsement, recommendation, or favoring by the U.S. Government or any agency thereof. The views and opinions of authors expressed herein do not necessarily state or reflect those of the U.S. Government or any agency thereof, and shall not be used for advertising or product endorsement purposes (LLNL-JRNL-812984).

- 
- [1] M. A. Barrios, D. G. Hicks, T. R. Boehly, D. E. Fratanduono, J. H. Eggert, P. M. Celliers, G. W. Collins, and D. D. Meyerhofer, *Phys. Plasmas* **17**, 056307 (2010).
  - [2] M. A. Barrios, T. R. Boehly, D. G. Hicks, D. E. Fratanduono, J. H. Eggert, G. W. Collins, and D. D. Meyerhofer, *J. Appl. Phys.* **111**, 093515 (2012).
  - [3] T. Döppner, D. C. Swift, A. L. Kritcher, B. Bachmann, G. W. Collins, D. A. Chapman, J. Hawreliak, D. Kraus, J. Nilsen, S. Rothman, L. X. Benedict, E. Dewald, D. E. Fratanduono, J. A. Gaffney, S. H. Glenzer, S. Hamel, O. L. Landen, H. J. Lee, S. LePape, T. Ma, M. J. MacDonald, A. G. MacPhee, D. Milathianaki, M. Millot, P. Neumayer, P. A. Sterne, R. Tommasini, and R. W. Falcone, *Phys. Rev. Lett.* **121**, 025001 (2018).
  - [4] A. L. Kritcher, T. Döppner, D. Swift, J. Hawreliak, J. Nilsen, J. Hammer, B. Bachmann, G. Collins, O. Landen, C. Keane, S. Glenzer, S. Rothman, D. Chapman, D. Kraus, and R. Falcone, *J. Phys.: Conf. Ser.* **688**, 012055 (2016).
  - [5] D. S. Clark, C. R. Weber, J. L. Milovich, J. D. Salmonson, A. L. Kritcher, S. W. Haan, B. A. Hammel, D. E. Hinkel, O. A. Hurricane, O. S. Jones, M. M. Marinak, P. K. Patel, H. F. Robey, S. M. Sepke, and M. J. Edwards, *Phys. Plasmas* **23**, 056302 (2016).
  - [6] S. Y. Gus'kov, N. N. Demchenko, N. V. Zmitrenko, D. V. Il'in, P. A. Kuchugov, V. B. Rozanov, V. E. Sherman, and R. A. Yakhin, *J. Russ. Laser Res.* **38**, 173 (2017).
  - [7] P. A. Sterne, L. X. Benedict, S. Hamel, A. A. Correa, J. L. Milovich, M. M. Marinak, P. M. Celliers, and D. E. Fratanduono, *J. Phys.: Conf. Ser.* **717**, 012082 (2016).
  - [8] A. S. Moore, S. Prisbrey, K. L. Baker, P. M. Celliers, J. Fry, T. R. Dittrich, K.-J. J. Wu, M. L. Kervin, M. E. Schoff, M. Farrell, A. Nikroo, and O. A. Hurricane, *J. Phys.: Conf. Ser.* **717**, 012038 (2016).
  - [9] R. E. Olson, G. A. Chandler, R. J. Leeper, A. Nobile, R. Wallace, J. A. Oertel, J. Faulkner, T. Archuletta, J. P. Knauer,

- R. E. Turner, K. Loughman, and V. Reki, in *Current Trends in International Fusion Research—Proceedings of the Fourth Symposium*, edited by C. D. Orth and E. Panarella (NRC Research Press, National Research Council of Canada, Ottawa, 2007), pp. 241–247.
- [10] A. J. MacKinnon, N. B. Meezan, J. S. Ross, S. Le Pape, L. Berzak Hopkins, L. Divol, D. Ho, J. Milovich, A. Pak, J. Ralph, T. Döppner, P. K. Patel, C. Thomas, R. Tommasini, S. Haan, A. G. MacPhee, J. McNaney, J. Caggiano, R. Hatarik, R. Bionta, T. Ma, B. Spears, J. R. Rygg, L. R. Benedetti, R. P. J. Town, D. K. Bradley, E. L. Dewald, D. Fittinghoff, O. S. Jones, H. R. Robey, J. D. Moody, S. Khan, D. A. Callahan, A. Hamza, J. Biener, P. M. Celliers, D. G. Braun, D. J. Erskine, S. T. Prisbrey, R. J. Wallace, B. Kozioziemski, R. Dylla-Spears, J. Sater, G. Collins, E. Storm, W. Hsing, O. Landen, J. L. Atherton, J. D. Lindl, M. J. Edwards, J. A. Frenje, M. Gatu-Johnson, C. K. Li, R. Petrasso, H. Rinderknecht, M. Rosenberg, F. H. Séguin, A. Zylstra, J. P. Knauer, G. Grim, N. Guler, F. Merrill, R. Olson, G. A. Kyrala, J. D. Kilkenny, A. Nikroo, K. Moreno, D. E. Hoover, C. Wild, and E. Werner, *Phys. Plasmas* **21**, 056318 (2014).
- [11] A. L. Kritcher, D. Clark, S. Haan, S. A. Yi, A. B. Zylstra, D. A. Callahan, D. E. Hinkel, L. F. Berzak Hopkins, O. A. Hurricane, O. L. Landen, S. A. MacLaren, N. B. Meezan, P. K. Patel, J. Ralph, C. A. Thomas, R. Town, and M. J. Edwards, *Phys. Plasmas* **25**, 056309 (2018).
- [12] A. B. Zylstra, S. MacLaren, S. A. Yi, J. Kline, D. Callahan, O. Hurricane, B. Bachmann, G. Kyrala, L. Masse, P. Patel, J. E. Ralph, J. Salmonson, P. Volegov, and C. Wilde, *Phys. Plasmas* **26**, 052707 (2019).
- [13] S. Zhang, B. Militzer, M. C. Gregor, K. Caspersen, L. H. Yang, J. Gaffney, T. Ogitsu, D. Swift, A. Lazicki, D. Erskine, R. A. London, P. M. Celliers, J. Nilsen, P. A. Sterne, and H. D. Whitley, *Phys. Rev. E* **98**, 023205 (2018).
- [14] A. C. Hayes, *Rep. Prog. Phys.* **80**, 026301 (2017).
- [15] R. Chen, Q. Shi, L. Su, M. Yang, Z. Huang, Y. Shi, Q. Zhang, Z. Liao, and T. Lu, *Ceramics Int.* **43**, 571 (2017).
- [16] S. Zhang, A. Lazicki, B. Militzer, L. H. Yang, K. Caspersen, J. A. Gaffney, M. W. Däne, J. E. Pask, W. R. Johnson, A. Sharma, P. Suryanarayana, D. D. Johnson, A. V. Smirnov, P. A. Sterne, D. Erskine, R. A. London, F. Coppari, D. Swift, J. Nilsen, A. J. Nelson, and H. D. Whitley, *Phys. Rev. B* **99**, 165103 (2019).
- [17] R. M. More, K. H. Warren, D. A. Young, and G. B. Zimmerman, *Phys. Fluids* **31**, 3059 (1988).
- [18] D. A. Young and E. M. Corey, *J. Appl. Phys.* **78**, 3748 (1995).
- [19] C. L. Ellison, H. D. Whitley, C. R. Brown, S. R. Copeland, W. J. Garbett, H. P. Le, M. B. Schneider, Z. B. Walters, H. Chen, J. I. Castor, R. S. Craxton, M. G. Johnson, E. M. Garcia, F. R. Graziani, G. E. Kemp, C. M. Krauland, P. W. McKenty, B. Lahmann, J. E. Pino, M. S. Rubery, H. A. Scott, R. Shepherd, and H. Sio, *Phys. Plasmas* **25**, 072710 (2018).
- [20] F. Thévenot, *J. Eur. Ceram. Soc.* **6**, 205 (1990).
- [21] T. Fujii, Y. Mori, H. Hyodo, and K. Kimura, *J. Phys.: Conf. Ser.* **215**, 012011 (2010).
- [22] P. Dera, M. H. Manghnani, A. Hushur, Y. Hu, and S. Tkachev, *J. Solid State Chem.* **215**, 85 (2014).
- [23] M. Chen, J. W. McCauley, and K. J. Hemker, *Science* **299**, 1563 (2003).
- [24] Y. Zhang, T. Mashimo, Y. Uemura, M. Uchino, M. Kodama, K. Shibata, K. Fukuoka, M. Kikuchi, T. Kobayashi, and T. Sekine, *J. Appl. Phys.* **100**, 113536 (2006).
- [25] T. J. Vogler, W. D. Reinhart, and L. C. Chhabildas, *J. Appl. Phys.* **95**, 4173 (2004).
- [26] V. Domnich, Y. Gogotsi, M. Trenary, and T. Tanaka, *Appl. Phys. Lett.* **81**, 3783 (2002).
- [27] D. Ge, V. Domnich, T. Juliano, E. Stach, and Y. Gogotsi, *Acta Mater.* **52**, 3921 (2004).
- [28] X. Q. Yan, W. J. Li, T. Goto, and M. W. Chen, *Appl. Phys. Lett.* **88**, 131905 (2006).
- [29] X. Q. Yan, Z. Tang, L. Zhang, J. J. Guo, C. Q. Jin, Y. Zhang, T. Goto, J. W. McCauley, and M. W. Chen, *Phys. Rev. Lett.* **102**, 075505 (2009).
- [30] D. E. Grady, *J. Appl. Phys.* **117**, 165904 (2015).
- [31] A. P. Awasthi and G. Subhash, *J. Appl. Phys.* **125**, 215901 (2019).
- [32] Q. An and W. A. Goddard, *Appl. Phys. Lett.* **110**, 111902 (2017).
- [33] P. Korotaev, A. Kuksin, P. Pokatashkin, and A. Yanilkin, *AIP Conf. Proc.* **1793**, 070014 (2017).
- [34] A. M. Molodets, A. A. Golyshev, and D. V. Shakhrai, *J. Exp. Theor. Phys.* **124**, 469 (2017).
- [35] A. Jay, O. Hardouin Duparc, J. Sjakste, and N. Vast, *J. Appl. Phys.* **125**, 185902 (2019).
- [36] D. E. Fratanduono, P. M. Celliers, D. G. Braun, P. A. Sterne, S. Hamel, A. Shamp, E. Zurek, K. J. Wu, A. E. Lazicki, M. Millot, and G. W. Collins, *Phys. Rev. B* **94**, 184107 (2016).
- [37] A. Shamp, E. Zurek, T. Ogitsu, D. E. Fratanduono, and S. Hamel, *Phys. Rev. B* **95**, 184111 (2017).
- [38] B. Wilson, V. Sonnad, P. Sterne, and W. Isaacs, *J. Quantum Spectrosc. Radiat. Transfer* **99**, 658 (2006).
- [39] B. Militzer, Ph.D. Thesis, University of Illinois at Urbana-Champaign, 2000.
- [40] D. M. Ceperley, *Rev. Mod. Phys.* **67**, 279 (1995).
- [41] C. Pierleoni, D. M. Ceperley, B. Bernu, and W. R. Magro, *Phys. Rev. Lett.* **73**, 2145 (1994).
- [42] K. P. Driver and B. Militzer, *Phys. Rev. Lett.* **108**, 115502 (2012).
- [43] V. Natoli and D. M. Ceperley, *J. Comp. Phys.* **117**, 171 (1995).
- [44] B. Militzer, *Comput. Phys. Commun.* **204**, 88 (2016).
- [45] H. K. Clark and J. L. Hoard, *J. Am. Chem. Soc.* **65**, 2115 (1943).
- [46] S. Zhang, K. P. Driver, F. Soubiran, and B. Militzer, *Phys. Rev. E* **96**, 013204 (2017).
- [47] S. Zhang, B. Militzer, L. X. Benedict, F. Soubiran, P. A. Sterne, and K. P. Driver, *J. Chem. Phys.* **148**, 102318 (2018).
- [48] P. E. Blöchl, O. Jepsen, and O. K. Andersen, *Phys. Rev. B* **49**, 16223 (1994).
- [49] D. R. Hamann, *Phys. Rev. B* **88**, 085117 (2013).
- [50] D. R. Hamann, *Phys. Rev. B* **95**, 239906(E) (2017).
- [51] S. Goedecker, *Rev. Mod. Phys.* **71**, 1085 (1999).
- [52] D. R. Bowler and T. Miyazaki, *Rep. Progr. Phys.* **75**, 036503 (2012).
- [53] G. Kresse and J. Furthmüller, *Phys. Rev. B* **54**, 11169 (1996).
- [54] J. P. Perdew, K. Burke, and M. Ernzerhof, *Phys. Rev. Lett.* **77**, 3865 (1996).
- [55] L. H. Yang, R. Q. Hood, J. E. Pask, and J. E. Klepeis, *J. Comput.-Aided Mater. Des.* **14**, 337 (2007).
- [56] S. Nosé, *J. Chem. Phys.* **81**, 511 (1984).
- [57] B. Militzer, *Phys. Rev. B* **79**, 155105 (2009).

- [58] K. P. Driver and B. Militzer, *Phys. Rev. B* **93**, 064101 (2016).
- [59] K. P. Driver, F. Soubiran, S. Zhang, and B. Militzer, *J. Chem. Phys.* **143**, 164507 (2015).
- [60] S. Zhang, K. P. Driver, F. Soubiran, and B. Militzer, *High Energ. Dens. Phys.* **21**, 16 (2016).
- [61] S. Zhang, K. P. Driver, F. Soubiran, and B. Militzer, *J. Chem. Phys.* **146**, 074505 (2017).
- [62] F. González-Cataldo, F. Soubiran, and B. Militzer, *Phys. Plasmas* **27**, 092706 (2020).
- [63] K. P. Driver, F. Soubiran, and B. Militzer, *Phys. Rev. E* **97**, 063207 (2018).
- [64] B. Militzer and K. P. Driver, *Phys. Rev. Lett.* **115**, 176403 (2015).
- [65] K. P. Driver and B. Militzer, *Phys. Rev. E* **95**, 043205 (2017).
- [66] F. Soubiran, F. González-Cataldo, K. P. Driver, S. Zhang, and B. Militzer, *J. Chem. Phys.* **151**, 214104 (2019).
- [67] F. González-Cataldo, F. Soubiran, H. Peterson, and B. Militzer, *Phys. Rev. B* **101**, 024107 (2020).
- [68] F. J. Rogers and H. E. DeWitt, *Phys. Rev. A* **8**, 1061 (1973).
- [69] F. J. Rogers, *Phys. Rev. A* **10**, 2441 (1974).
- [70] F. J. Rogers, *Phys. Rev. A* **19**, 375 (1979).
- [71] F. J. Rogers, *Phys. Rev. A* **24**, 1531 (1981).
- [72] D. Johnson, A. Smirnov, and S. Khan, *MECCA: Multiple-scattering Electronic-structure Calculations for Complex Alloys (KKR-CPA Program, ver. 2.0)* (Iowa State University and Ames Laboratory, Ames, 2015).
- [73] S. H. Vosko, L. Wilk, and M. Nusair, *Can. J. Phys.* **58**, 1200 (1980).
- [74] H. J. Monkhorst and J. D. Pack, *Phys. Rev. B* **13**, 5188 (1976).
- [75] E. I. Moses, R. N. Boyd, B. A. Remington, C. J. Keane, and R. Al-Ayat, *Phys. Plasmas* **16**, 041006 (2009).
- [76] The B<sub>4</sub>C samples were created through a sintering process and characterized using a combination of x-ray diffraction, focused ion beam (FIB), energy dispersive spectroscopy (EDS), and measurements of volume and mass to determine density. The material was polycrystalline with high purity and randomly oriented grains. FIB analysis revealed some isolated micron-scale graphitic inclusions and submicron scale voids which reduced the bulk density from the theoretical value of 2.52 to 2.51 g/cm<sup>3</sup>.
- [77] P. M. Celliers, D. K. Bradley, G. W. Collins, D. G. Hicks, T. R. Boehly, and W. J. Armstrong, *Rev. Sci. Instrum.* **75**, 4916 (2004).
- [78] D. E. Fratanduono, D. H. Munro, P. M. Celliers, and G. W. Collins, *J. Appl. Phys.* **116**, 033517 (2014).
- [79] L. X. Benedict, K. P. Driver, S. Hamel, B. Militzer, T. Qi, A. A. Correa, A. Saul, and E. Schwegler, *Phys. Rev. B* **89**, 224109 (2014).
- [80] M. C. Gregor, D. E. Fratanduono, C. A. McCoy, D. N. Polsin, A. Sorce, J. R. Rygg, G. W. Collins, T. Braun, P. M. Celliers, J. H. Eggert, D. D. Meyerhofer, and T. R. Boehly, *Phys. Rev. B* **95**, 144114 (2017).
- [81] M. Millot, P. A. Sterne, J. H. Eggert, S. Hamel, M. C. Marshall, and P. M. Celliers, *Phys. Plasmas* **27**, 102711 (2020).
- [82] M. Millot, P. M. Celliers, P. A. Sterne, L. X. Benedict, A. A. Correa, S. Hamel, S. J. Ali, K. L. Baker, L. F. Berzak Hopkins, J. Biener, G. W. Collins, F. Coppari, L. Divol, A. Fernandez-Panella, D. E. Fratanduono, S. W. Haan, S. Le Pape, N. B. Meezan, A. S. Moore, J. D. Moody, J. E. Ralph, J. S. Ross, J. R. Rygg, C. Thomas, D. P. Turnbull, C. Wild, and J. H. Eggert, *Phys. Rev. B* **97**, 144108 (2018).
- [83] M. C. Marshall, A. E. Lazicki, D. Erskine, R. A. London, D. E. Fratanduono, P. M. Celliers, J. H. Eggert, F. Coppari, D. C. Swift, P. A. Sterne, H. D. Whitley, and J. Nilsen, *Phys. Rev. B* **99**, 174101 (2019).
- [84] Materials Project database, mp-696746.
- [85] See <http://opium.sourceforge.net> for information about the OPIUM code.
- [86] L. Kleinmann, *AIP Conf. Proc.* **231**, 13 (1991).
- [87] A. L. Kritcher, D. C. Swift, T. Döppner, B. Bachmann, L. X. Benedict, G. W. Collins, J. L. DuBois, F. Elsner, G. Fontaine, J. A. Gaffney, S. Hamel, A. Lazicki, W. R. Johnson, N. Kostinski, D. Kraus, M. J. MacDonald, B. Maddox, M. E. Martin, P. Neumayer, A. Nikroo, J. Nilsen, B. A. Remington, D. Saumon, P. A. Sterne, W. Sweet, A. A. Correa, H. D. Whitley, R. W. Falcone, and S. H. Glenzer, *Nature* **584**, 51 (2020).
- [88] A. Lazicki, D. Swift *et al.* (private communication).
- [89] See Supplemental Material at <http://link.aps.org/supplemental/10.1103/PhysRevE.102.053203> for the EOS data table of B<sub>4</sub>C from this study.
- [90] J. A. Gaffney, S. T. Brandon, K. D. Humbird, M. K. G. Kruse, R. C. Nora, J. L. Peterson, and B. K. Spears, *Phys. Plasmas* **26**, 082704 (2019).
- [91] H. D. Whitley, G. E. Kemp, C. Yeaman, Z. Walters, B. E. Blue, W. Garbett, M. Schneider, R. S. Craxton, E. M. Garcia, P. W. McKenty, M. Gatu-Johnson, K. Caspersen, J. I. Castor, M. Däne, C. L. Ellison, J. Gaffney, F. R. Graziani, J. Klepeis, N. Kostinski, A. Kritcher, B. Lahmann, A. E. Lazicki, H. P. Le, R. A. London, B. Maddox, M. Marshall, M. E. Martin, B. Militzer, A. Nikroo, J. Nilsen, T. Ogitsu, J. Pask, J. E. Pino, M. Rubery, R. Shepherd, P. A. Sterne, D. C. Swift, L. Yang, and S. Zhang, [arXiv:2006.15635](https://arxiv.org/abs/2006.15635).
- [92] C. Yeaman, G. Kemp, Z. Walters, H. Whitley, P. McKenty, E. Garcia, Y. Yang, R. Craxton, and B. E. Blue, High yield polar direct drive fusion neutron sources at the national ignition facility (unpublished).
- [93] M. P. Allen and D. J. Tildesley, *Computer Simulation of Liquids* (Oxford Science Publications, Oxford, UK, 1987).
- [94] The 5-atom structure has four B forming a face-centered cubic lattice and one C at the body center of the cell; the 10-atom structure consists of two C forming a body-centered cubic lattice that is centered at (0, 0, 0) and interconnects with eight B atoms that occupy the ( $\pm 1/4$ ,  $\pm 1/4$ ,  $\pm 1/4$ ) sites and form a simple-cubic lattice; the 15-atom structure is a pseudo-rhombohedral phase of B<sub>4</sub>C consisting of a boron icosahedra and a carbon chain.
- [95] D. Swift, J. Hawreliak, D. Braun, A. Kritcher, S. Glenzer, G. W. Collins, S. Rothman, D. Chapman, and S. Rose, *AIP Conf. Proc.* **1426**, 477 (2012).
- [96] J. Nilsen, B. Bachmann, G. Zimmerman, R. Hatarik, T. Döppner, D. Swift, J. Hawreliak, G. Collins, R. Falcone, S. Glenzer *et al.*, *High Energ. Dens. Phys.* **21**, 20 (2016).
- [97] D. C. Swift, A. L. Kritcher, J. A. Hawreliak, A. Lazicki, A. MacPhee, B. Bachmann, T. Döppner, J. Nilsen, G. W. Collins, S. Glenzer, S. D. Rothman, D. Kraus, and R. W. Falcone, *Rev. Sci. Instrum.* **89**, 053505 (2018).